

See discussions, stats, and author profiles for this publication at: <https://www.researchgate.net/publication/245425590>

# Oscillation Frequency and Amplitude Effects on the Wake of a Plunging Airfoil

Article in AIAA Journal · October 2004

DOI: 10.2514/1.5070

---

CITATIONS  
280

2 authors:



John Young  
UNSW Sydney  
136 PUBLICATIONS 3,883 CITATIONS

[SEE PROFILE](#)

---

READS  
2,429



Joseph C. S. Lai  
UNSW Sydney  
303 PUBLICATIONS 7,411 CITATIONS

[SEE PROFILE](#)

# Oscillation Frequency and Amplitude Effects on the Wake of a Plunging Airfoil

J. Young\* and J. C. S. Lai†

University of New South Wales, Canberra, Australian Capital Territory 2600, Australia

The flow over a NACA 0012 airfoil, oscillated sinusoidally in plunge, is simulated numerically using a compressible two-dimensional Navier-Stokes solver at a Reynolds number of  $2 \times 10^4$ . The wake of the airfoil is visualized using a numerical particle tracing method. Close agreement is obtained between numerically simulated wake structures and experimental wake visualizations in the literature, when the flow is assumed to be fully laminar. The wake structures, and the lift and thrust of the airfoil, are shown to be strongly dependent on both the Strouhal number and the reduced frequency  $k$  of the plunge oscillation at this Reynolds number. Leading-edge separation appears to dominate the generation of aerodynamic forces for reduced frequencies below approximately  $k = 4$  but becomes secondary for higher frequencies. Wake structures appear to be controlled primarily by trailing-edge effects at all frequencies tested up to  $k = 20$ . Aerodynamic force results obtained at this Reynolds number show marked differences from those predicted by potential flow analyses at low plunge frequency and high amplitude but are similar at high frequency and low amplitude, consistent with the effect of leading-edge separation.

## Nomenclature

$a$	= single-sided plunge amplitude
$a_\infty$	= freestream speed of sound
$C_{L\text{peak}}$	= single-sided-peak lift coefficient per unit span
$C_{T\text{mean}}$	= time-averaged thrust coefficient per unit span
$c$	= airfoil chord
$f$	= plunge frequency, Hz
$h$	= nondimensional plunge amplitude, $a/c$
$k$	= reduced frequency, $\omega c/(2U_\infty)$
$M_\infty$	= freestream Mach number
$Re$	= Reynolds number based on airfoil chord
$Sr$	= Strouhal number based on trailing edge excursion, $2af/U_\infty = 2kh/\pi$
$T$	= nondimensional plunge period, $2\pi a_\infty/(\omega c) = \pi/(kM_\infty)$
$U_\infty$	= freestream velocity
$\alpha$	= pitch amplitude
$\omega$	= angular frequency, $2\pi f$

## Introduction

OSCILLATING airfoils have been extensively studied both numerically and experimentally, in contexts such as the dynamics of the wake and vortex rollup,<sup>1</sup> the dynamic stall phenomenon,<sup>2–4</sup> details of fish and marine mammal propulsion,<sup>5–7</sup> the use of oscillating airfoils in flow control and flow reattachment,<sup>8,9</sup> and the use of flapping wings for generation of lift and propulsion in micro air vehicles.<sup>10</sup> Early theoretical analyses and a number of experimental studies<sup>11–13</sup> have shown that oscillating airfoils generate thrust at certain combinations of oscillation frequency and amplitude. Garrick<sup>14</sup> determined the propulsive efficiency of a plunging and pitching flat-plate airfoil as a function of the oscillation frequency, with the assumption of potential flow and small-amplitude

Received 9 September 2003; revision received 24 December 2003; accepted for publication 28 January 2004. Copyright © 2004 by J. Young and J. C. S. Lai. Published by the American Institute of Aeronautics and Astronautics, Inc., with permission. Copies of this paper may be made for personal or internal use, on condition that the copier pay the \$10.00 per-copy fee to the Copyright Clearance Center, Inc., 222 Rosewood Drive, Danvers, MA 01923; include the code 0001-1452/04 \$10.00 in correspondence with the CCC.

\*Graduate Student, School of Aerospace, Civil and Mechanical Engineering, Australian Defence Force Academy; j.young@adfa.edu.au. Member AIAA.

†Professor, School of Aerospace, Civil and Mechanical Engineering, Australian Defence Force Academy; j.lai@adfa.edu.au. Senior Member AIAA.

oscillation. Although pure plunging airfoil motion has received relatively less attention than pitching motion, Freymuth,<sup>15</sup> Jones et al.<sup>16</sup> and Lai and Platzer<sup>17</sup> show that the wakes of plunging airfoils can be characterized as drag-producing, neutral, or thrust-producing depending on the plunge frequency and amplitude. Drag-producing wakes have velocity profiles that show a momentum deficit when time averaged, typically with von Kármán vortex street wake configurations with two alternating vortex rows, clockwise above and anticlockwise below (flow from left to right as in Fig. 1). Vortex pairs form mushroomlike structures that are tilted upstream. Thrust-producing wakes show a momentum surfeit, or jet, superimposed on the momentum-deficit velocity profile in the time-averaged flow, such that the thrust of the jet is greater than the inherent drag of the airfoil. The wake configuration is typically a reverse von Kármán vortex street with two rows of alternating vortices, anticlockwise above and clockwise below, so that vortex pairs form downstream-tilted mushrooms. Neutral wakes, where the thrust due to plunging balances the inherent drag, may show multiple vortex shedding per half-cycle, and vortex pairs are not tilted. The vortex-shedding process that leads to the described wake patterns, and to the generation of lift and thrust, is not well understood.

The objective of this study is to explore the details of wake structure formation, lift, and thrust generation, and their dependency on plunging frequency and amplitude, for an airfoil undergoing pure sinusoidal plunging motion. A Navier-Stokes flow solver, in combination with a numerical particle tracing method, is validated against experimental and computational results in the literature for pitching and plunging airfoils. An unsteady panel method solver is also used to isolate and determine the relative importance of elements of the controlling physics.

## Linearized Analysis

For a plunging flat plate, Garrick,<sup>14</sup> using linearized potential flow theory, determines the time-averaged thrust coefficient per unit span  $C_{T\text{mean}}$ , and the single-sided peak lift coefficient per unit span  $C_{L\text{peak}}$ , as a function of the nondimensional plunge amplitude  $h$  and reduced frequency  $k$ :

$$C_{T\text{mean}} = 4\pi(kh)^2 A, \quad A = (F^2 + G^2)$$

$$C_{L\text{peak}} = 4\pi(kh)B, \quad B = (F^2 + G^2 + kG + k^2/4)^{\frac{1}{2}} \quad (1)$$

where  $F = F(k)$  and  $G = G(k)$  are the real and imaginary components of the Theodorsen function  $C(k) = F(k) + iG(k)$ . The  $A$  term asymptotes to a constant value 0.25 for large  $k$  (approximately  $k > 4.0$ ), so that  $C_{T\text{mean}}$  depends only on the single parameter  $kh$ .

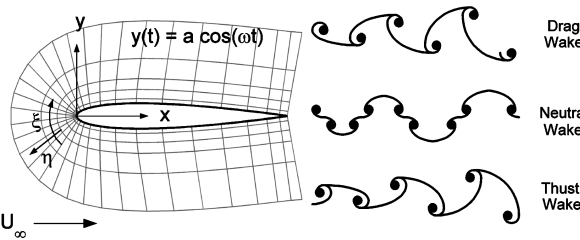


Fig. 1 Plunging two-dimensional NACA 0012 airfoil in infinite steady freestream flow.

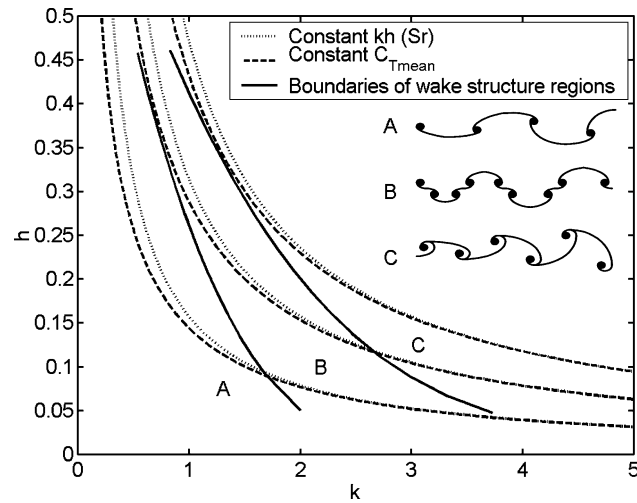


Fig. 2 Variation of constant average thrust coefficient with  $k$  and  $h$ , predicted by linearized potential theory<sup>14</sup> and experimentally derived regions of differing wake structure.<sup>6,19,20</sup>

for large enough  $k$ . Lines of constant average thrust coefficient in a plot of  $h$  vs  $k$  asymptote to lines of constant  $kh$  (equivalent to constant Strouhal number based on total trailing edge motion because  $kh = Sr \times \pi/2$ ) as shown in Fig. 2. The  $B$  term asymptotes to  $k/2$  for large  $k$ .

Note that expression (1) assumes that the wake consists of a continuous sinusoidal vortex sheet with a small wake width, that is,  $h \rightarrow 0$ . Therefore, the lines of constant average thrust coefficient in Fig. 2 are valid only for small  $h$ . Additionally the potential theory does not allow the wake to develop, so that nonlinearities due to self-induced evolution of the wake are not taken into account. A third assumption of the theoretical approach by Garrick is that the Kutta condition is satisfied at the trailing edge. The limited validity of this assumption for oscillating airfoils is discussed by McCroskey<sup>18</sup> and illustrated by results presented later in this paper.

Expression (1) would imply that for large  $k$ , for instance,  $k > 4.0$ , two flows with the same  $kh$ , but differing values of  $k$  and  $h$ , should have the same vortex structure in the wake and develop the same average thrust coefficient. However, as shown in Fig. 2, approximate boundaries separating the regions of different wake shapes, determined experimentally,<sup>6,19,20</sup> do not closely follow either lines of constant average thrust coefficient predicted by the potential theory or lines of constant  $kh$ . In fact the difference in behavior is most marked for low plunge amplitude  $h$ , where the thin-wake assumption of the potential theory has its greatest validity. This suggests that the linearized theory is insufficient to explain the observed phenomena and, furthermore, that  $kh$  (or Strouhal number  $Sr$ ) cannot be regarded as the single parameter determining the shape of the wake and the thrust developed. Rather, both the reduced frequency of plunging  $k$  and the amplitude of motion  $h$  must be considered as separate parameters. This is explored further in this study.

## Numerical Method

### Navier-Stokes Solver

The strong-conservation form of the nondimensionalized two-dimensional unsteady compressible Reynolds averaged Navier-Stokes (N-S) equations is, in generalized coordinates,

$$\frac{\partial \hat{Q}}{\partial \tau} + \frac{\partial \hat{F}}{\partial \xi} + \frac{\partial \hat{G}}{\partial \eta} = \frac{\partial \hat{R}}{\partial \xi} + \frac{\partial \hat{S}}{\partial \eta} \quad (2)$$

with  $\hat{Q} = (\rho, \rho u, \rho v, e)/J$  the vector of conserved variables,  $\hat{F}$  and  $\hat{G}$  the inviscid fluxes,  $\hat{R}$  and  $\hat{S}$  the viscous fluxes,  $\xi$  and  $\eta$  the generalized coordinates, and  $\tau$  the nondimensional time. These equations may be rewritten to include explicitly the variation of the Jacobian of the coordinate transformation  $J$ , with time,

$$\frac{\partial Q}{\partial \tau} + J \frac{\partial \hat{F}}{\partial \xi} + J \frac{\partial \hat{G}}{\partial \eta} = J \frac{\partial \hat{R}}{\partial \xi} + J \frac{\partial \hat{S}}{\partial \eta} + \frac{Q}{J} \frac{\partial J}{\partial \tau} \quad (3)$$

with  $Q = J \hat{Q}$ . The equations are solved on a structured  $C$  grid wrapped around the airfoil, as shown in Fig. 1. The plunging and pitching motion of the airfoil is introduced by deforming the grid adjacent to the airfoil, which results in a time-dependent Jacobian and grid metrics.

The code generally follows the method of Tuncer and Platzer,<sup>21</sup> with some modifications. The numerical method uses Crank-Nicolson second-order time discretization. Viscous flux terms are evaluated using second-order central differences in space and inviscid fluxes with a third-order accurate Osher upwind scheme. The resulting semi-implicit equations are nonlinear in  $Q^{n+1}$  (the solution at the next time step), which is solved for using approximate factorization and Newton subiteration. Typically, two iterations were found sufficient, at which time  $Q^{n+1}$  is approximated by  $Q^{p+1}$  (where superscript  $n$  represents the time level and  $p$  is a subiteration counter):

$$\begin{aligned} & \left[ I + \frac{\Delta \tau}{2} J \frac{\partial}{\partial \xi} \hat{A} \right]^p \left[ I + \frac{\Delta \tau}{2} J \left\{ \frac{\partial}{\partial \eta} \hat{B} - \frac{\partial}{\partial \eta} \hat{N} \right\} \right]^p (Q^{p+1} - Q^p) \\ &= -(Q^p - Q^n) + \frac{\Delta \tau}{2} J^p \left[ - \frac{\partial \hat{F}}{\partial \xi} - \frac{\partial \hat{G}}{\partial \eta} + \frac{\partial \hat{R}}{\partial \xi} + \frac{\partial \hat{S}}{\partial \eta} \right]^p \\ &+ \frac{\Delta \tau}{2} J^n \left[ - \frac{\partial \hat{F}}{\partial \xi} - \frac{\partial \hat{G}}{\partial \eta} + \frac{\partial \hat{R}}{\partial \xi} + \frac{\partial \hat{S}}{\partial \eta} \right]^n \\ &+ \frac{Q^p + Q^n}{J^p + J^n} (J^p - J^n) \end{aligned} \quad (4)$$

The Newton subiteration process involves formulation of the inviscid and viscous flux-Jacobian matrices:

$$\hat{A} = \frac{\partial \hat{F}}{\partial Q}, \quad \hat{B} = \frac{\partial \hat{G}}{\partial Q}, \quad \hat{M} = \frac{\partial \hat{R}}{\partial Q}, \quad \hat{N} = \frac{\partial \hat{S}}{\partial Q} \quad (5)$$

The method by Tuncer and Platzer<sup>21</sup> uses the thin-layer approximation,<sup>22</sup> thereby ignoring the streamwise viscous derivative  $\partial \hat{R}/\partial \xi$ , any cross-derivatives in the  $\partial \hat{S}/\partial \eta$  term, and the flux-Jacobian  $\hat{M}$ . To account for all viscous effects more fully without sacrificing computational speed, the current method retains all viscous terms on the right-hand side of the equations. However,  $\hat{M}$  is still ignored on the left-hand side. It may be seen that as the subiterations at each time step proceed,  $Q^{p+1}$  approaches  $Q^p$ , the left-hand side vanishes, and the full viscous equations are recovered. Inflow and outflow boundary conditions are implemented using second-order Riemann invariant extrapolations. The method is, thus, overall second-order in time and space. Turbulent calculations are performed using the Baldwin-Lomax algebraic turbulence model.<sup>22</sup> The code is also parallelized using OpenMP for shared memory architectures.

Scalar particle tracing is performed by releasing particles at locations fixed relative to the airfoil trailing edge, and particle paths

are integrated in  $(\xi, \eta)$  grid coordinates. Physical velocities  $(u, v)$  at the corners of the current cell, determined by the particle  $(\xi, \eta)$  grid coordinates, are converted to equivalent velocities in the  $(x, y)$  domain via the expression

$$\begin{aligned}\dot{\xi} &= \frac{\partial \xi}{\partial x} \left( u - \frac{\partial x}{\partial \tau} \right) + \frac{\partial \xi}{\partial y} \left( v - \frac{\partial y}{\partial \tau} \right) \\ \dot{\eta} &= \frac{\partial \eta}{\partial x} \left( u - \frac{\partial x}{\partial \tau} \right) + \frac{\partial \eta}{\partial y} \left( v - \frac{\partial y}{\partial \tau} \right)\end{aligned}\quad (6)$$

where  $\partial x/\partial \tau$  and  $\partial y/\partial \tau$  are the grid deformation rates and  $\partial \xi/\partial x$ ,  $\partial \xi/\partial y$ ,  $\partial \eta/\partial x$ , and  $\partial \eta/\partial y$  are grid metrics taken to be uniform across a cell. The particle equivalent  $(\xi, \eta)$  velocity is calculated by bilinear interpolation of the cell corner values, based on the current  $(\xi, \eta)$  coordinates. The new  $(\xi, \eta)$  particle location is calculated with a fourth-order predictor-corrector method. If adjacent cells are not identical, that is, the grid is nonuniform, differing grid metrics in the cells will introduce an error as a particle crosses the cell boundary, unless care is taken to recalculate  $\dot{\xi}$  and  $\dot{\eta}$  based on the new cell grid metrics for the remainder of that time step. The new  $(x, y)$  particle location is determined by bilinear interpolation of the position values at the corners of the new cell, based on the new  $(\xi, \eta)$  grid coordinates.

The particle tracing method was verified for steady potential flow around a cylinder, where it was found to reproduce accurately the calculated streamlines. It was also compared to integration of particle paths in the  $(x, y)$  domain for unsteady flow and found to produce indistinguishable results for the grid size and time steps used in the current work. For the cases run here,  $(\xi, \eta)$  domain tracing added up to 20% overhead to the fluid solver calculations, whereas  $(x, y)$  domain tracing added up to 300% overhead due to the computationally intensive requirement to locate the grid cell containing the particle being integrated, for every particle at each time step.

#### Unsteady Panel Method Solver

To isolate and compare elements of the controlling physics of the plunging airfoil flow, an unsteady panel method (UPM) code was also developed, following Basu and Hancock<sup>23</sup> and Jones et al.<sup>24</sup> The method assumes potential flow and enforces the Kutta condition at the trailing edge, as per the Garrick<sup>14</sup> analysis, and so does not allow any separation over the airfoil surface. However, as the airfoil translates and the lift changes, vorticity is shed into the wake at each time step, and this is allowed to evolve due to self-induced velocities. Thus, the nonlinear character of the wake, and any consequent effect on lift and thrust, is preserved. The UPM code also accounts for airfoil thickness, which the Garrick analysis does not. The code was tested against, and accurately reproduced, both wake shapes and thrust coefficient results for the panel method used by Jones et al.<sup>24</sup>

### N-S Code Verification and Validation

#### Pitching Airfoil

Experiments were performed by Koochesfahani<sup>12</sup> and numerical simulations by Ramamurti and Sandberg<sup>25</sup> for a NACA 0012 airfoil pitching about the quarter-chord point, at Reynolds number  $Re = 12 \times 10^4$ , and these results were used to validate the N-S solver. The N-S code was run with pitch amplitudes  $\alpha = \pm 2$  and  $\alpha = \pm 4$  deg, reduced pitching frequencies of  $k = 1-12$ , and Mach number  $M_\infty = 0.2$  and  $M_\infty = 0.05$  to check sensitivity of results to Mach number effects. The flow for the calculations was assumed to be laminar at this Reynolds number. The computational grid consisted of  $541 \times 61$  normal points, with 189 points along the airfoil surface, and the first normal point at a distance of  $8.75 \times 10^{-6}$  of a chord-length from the airfoil surface. There were typically upward of 30 normal points in the boundary layer at the trailing edge. All oscillating flow calculations were started from fully converged stationary airfoil solutions. Convergence times increased significantly with decreasing freestream Mach number, as expected for a compressible flow solver.<sup>26,27</sup> For oscillating airfoil

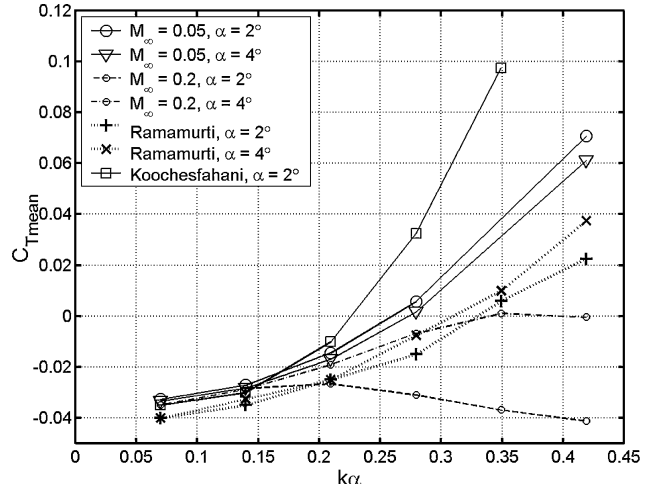


Fig. 3 Mean thrust coefficient, NACA 0012 airfoil pitching about quarter-chord,  $Re = 1.2 \times 10^4$ .

calculations, transients in aerodynamic forces were observed to disappear, typically within five cycles of motion, for both  $M_\infty = 0.05$  and  $M_\infty = 0.2$ . A time step of  $\Delta \tau = 4.7 \times 10^{-4}$  was used, resulting in from 1100 to over 13,000 time steps per cycle of airfoil motion, depending on the pitching frequency. The thrust coefficient (negative of the drag coefficient) was calculated by integrating pressure and shear stress around the airfoil surface, and the result was time averaged once transients in the simulation had died down and the thrust time history had become sinusoidal.

Figure 3 shows the comparison with the calculations by Ramamurti and Sandberg<sup>25</sup> using an incompressible finite elements solver, and the experiments by Koochesfahani.<sup>12</sup> We see that with  $M_\infty = 0.05$ , the N-S code reproduces the same trend observed by Ramamurti and Sandberg, in that thrust is approximately dependent on the product  $k\alpha$  rather than  $k$  or  $\alpha$  individually. The N-S code is also closer to the experimental values observed by Koochesfahani, particularly at low values of  $k\alpha$ , although it still underpredicts the thrust. Potential sources of error in the Koochesfahani observations are discussed by Ramamurti and Sandberg<sup>25</sup> and Jones and Platzer.<sup>28</sup> Note that for  $M_\infty = 0.2$  the N-S code shows very different behavior in Fig. 3. At this freestream Mach number, the flow cannot really be considered incompressible due to large velocities induced over the airfoil during the pitching cycle. Also because velocities in the code are nondimensionalized by the freestream speed of sound, pressure waves have a wavelength inversely proportional to the product of the freestream Mach number  $M_\infty$  and the oscillation reduced frequency  $k$ . For  $M_\infty = 0.2$  and  $k = 12$ , the wavelength is approximately one airfoil chord. This leads to an interaction between pressure waves and the airfoil, which was negligible for  $M_\infty = 0.05$  for all of the frequencies under consideration, but was apparent for  $M_\infty = 0.2$  at the higher frequencies. The net result is significant differences in pressure distribution at the nose of the airfoil between the two Mach numbers.

As further validation, a stationary NACA 0012 airfoil at  $Re = 1.2 \times 10^4$  was considered. Koochesfahani<sup>12</sup> measured a natural vortex-shedding frequency in the wake equivalent to  $k = 8.7$ , which was reproduced by the N-S code here.

Grid and time step refinement was carried out for an airfoil pitching about the quarter chord, at Reynolds number  $Re = 1.2 \times 10^4$ , reduced frequency  $k = 8.0$ , and pitch amplitude  $\alpha = \pm 2$  deg, again for Mach numbers  $M_\infty = 0.2$  and  $M_\infty = 0.05$ . The grids and time steps used were  $541 \times 61$  points (189 points along the airfoil,  $\Delta \tau = 4.7 \times 10^{-4}$ ),  $1081 \times 61$  (377 points along the airfoil,  $\Delta \tau = 6.8 \times 10^{-5}$ ),  $2161 \times 61$  (753 points along the airfoil,  $\Delta \tau = 6.6 \times 10^{-5}$ ), and  $1081 \times 121$  (377 points along the airfoil,  $\Delta \tau = 8.8 \times 10^{-5}$ ). It was found that the  $541 \times 61$  grid was sufficiently refined and that the lift and thrust coefficients were grid independent (Fig. 4).

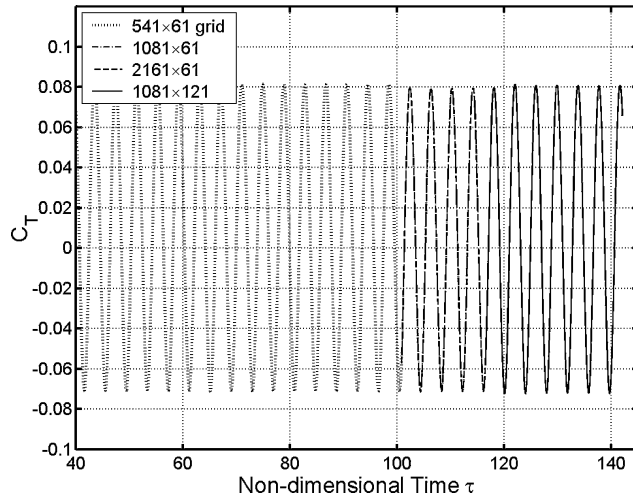


**Fig. 4** Thrust coefficient time histories, NACA 0012 airfoil pitching about quarter-chord,  $Re = 1.2 \times 10^4$ ,  $M_\infty = 0.05$ ,  $k = 8.0$ , and  $\alpha = \pm 2$  deg.

The pitch angles used in the pitching airfoil validation resulted in trailing-edge excursions of  $\pm 0.026$  and  $\pm 0.053$  chords, which are in the range of the plunging motions considered hereafter. Also the equivalent  $kh$  (considering the trailing edge motion only) of these cases was in the range 0.05–0.31, which corresponds to the range used in the plunging calculations.

#### Plunging Airfoil Wake Structures: Grid and Time Step Refinement

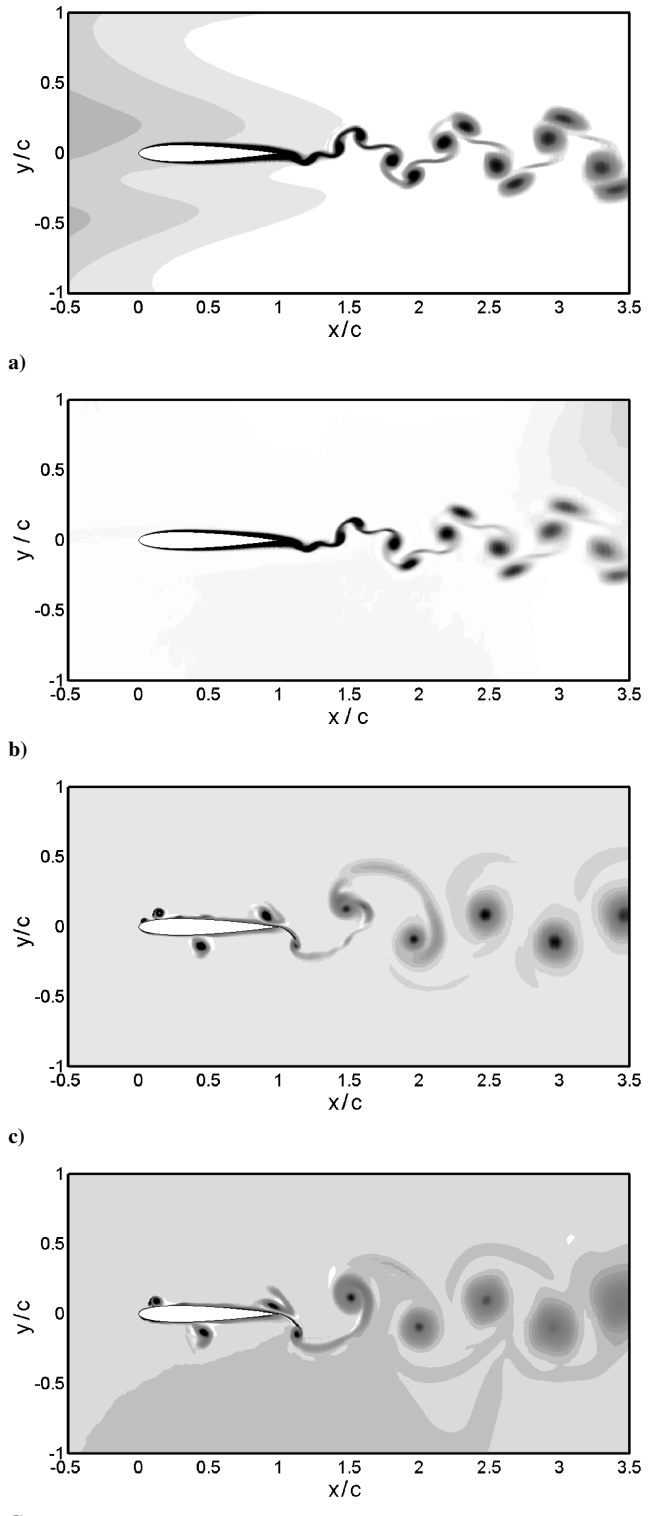
Further investigation was performed for a purely plunging airfoil, to determine the level of grid refinement necessary to make lift and thrust coefficient results and wake structures grid independent and to determine the effect of freestream Mach number. Two different combinations of plunging frequency and amplitude, giving rise to very different wake structures, were chosen for this comparison.

Figure 5 shows filled-contour plots of the entropy  $s = p/\rho^\gamma$  in the airfoil wake, for the cases  $k = 4.0$ ,  $h = 0.0125$  and  $k = 4.0$ ,  $h = 0.075$ , for  $M_\infty = 0.2$  and  $M_\infty = 0.05$ . It may be seen that the two different freestream Mach numbers gave rise to very similar vortex shedding and wake structures, even though the forces generated by the airfoil were quite different in line with the pitching airfoil validation.

As in the case of the pitching validation, grid and time step refinement was performed until the aerodynamic forces, vortex-shedding phenomena, and wake structures in the airfoil near-field became grid independent, for the  $k = 4.0$ ,  $h = 0.0125$  case. A number of different grids, with  $541 \times 61$ ,  $1081 \times 61$ ,  $2161 \times 61$ ,  $541 \times 121$ ,  $1081 \times 121$ ,  $2161 \times 121$ , and  $1081 \times 241$  points, were used in this refinement study. An increase in required grid resolution was found with decreasing Mach number, from the  $1081 \times 61$  grid for  $M_\infty = 0.2$ , to the  $1081 \times 121$  grid for  $M_\infty = 0.05$ , which was as expected from published low Mach number compressible code results.<sup>26,27</sup>

#### Particle Tracing Validation

Figure 6 shows that the scalar particles, introduced to the flow along a vertical line at the trailing edge of the airfoil, follow the contours of vorticity and entropy very closely. Note that the hyperbolic tangent of the vorticity, rather than the vorticity itself, has been plotted to scale the data for ease of viewing. The scalar particle traces are used hereafter rather than vorticity or entropy contour plots, because fine details of the wake structure may be more easily discerned in the particle traces. Note also that particles are released from arbitrarily defined points in the flow, not necessarily from grid points, so that density of particles does not indicate density of grid points.



**Fig. 5** Entropy filled-contour plots, plunging airfoil,  $Re = 2 \times 10^4$ , laminar: a)  $k = 4.0$ ,  $h = 0.0125$ , and  $M_\infty = 0.2$ ; b)  $M_\infty = 0.05$ ; c)  $k = 4.0$ ,  $h = 0.075$ , and  $M_\infty = 0.2$ ; and d)  $M_\infty = 0.05$ .

#### Wake Visualization Results

Numerical results were generated for a number of  $k$  and  $h$  values, at a Reynolds number  $Re = 2 \times 10^4$  and Mach number  $M_\infty = 0.2$ , under both fully laminar and fully turbulent flow assumptions. Experimental results generated in a water tunnel at  $Re = 2 \times 10^4$ , are reproduced from Lai and Platzer.<sup>17</sup> Note that the backgrounds of the experimental visualizations have been processed to highlight details of the wake structure.

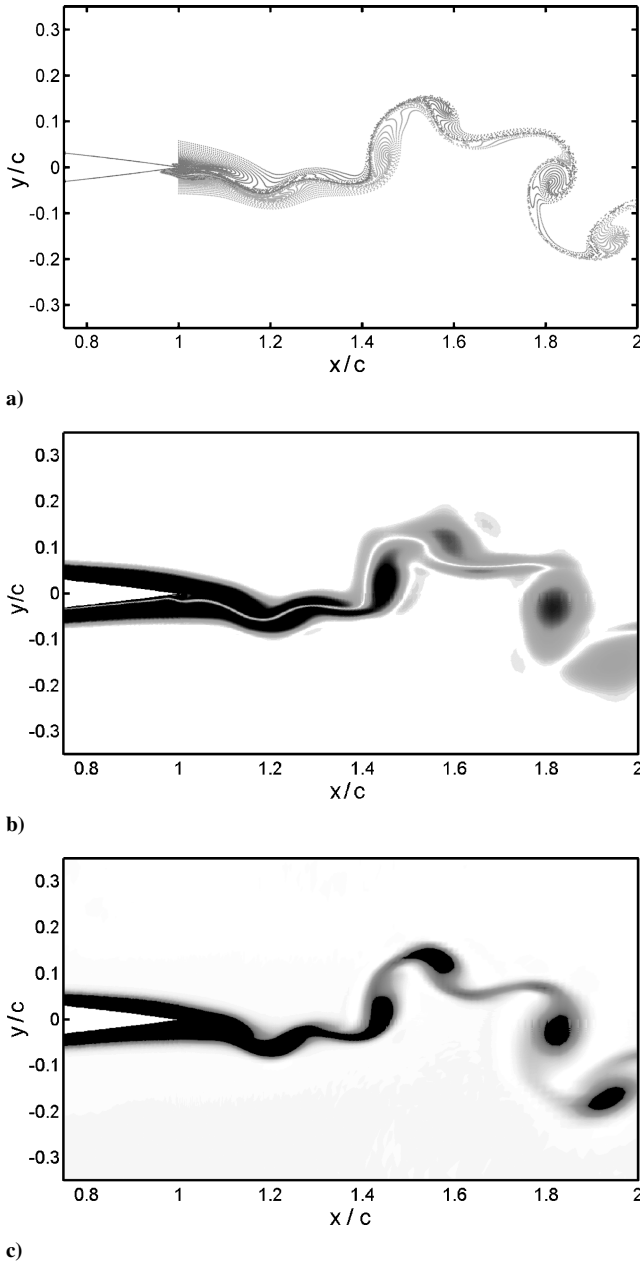


Fig. 6 Plunging airfoil,  $Re = 2 \times 10^4$ ,  $k = 4.0$ ,  $h = 0.0125$ , laminar, and  $M_\infty = 0.05$ : a) particle trace, b) hyperbolic tangent of vorticity filled-contour plot, and c) entropy filled-contour plot.

Figure 7 shows a comparison of experimental and numerical results at  $k \approx 4.0$  and  $h = 0.0125$ . The fully laminar numerical results reproduce the same qualitative aspects of the experimental wake vortex structure, with two roughly equal strength same-sign vortices shed per half-cycle of airfoil motion and upstream-tilted vortex pairs indicative of net drag (confirmed by averaged flowfield calculations showing a momentum-deficit wake aft of the trailing edge). The fully turbulent numerical results are qualitatively different, and although there are still two same-sign vortices shed per half-cycle, they are now of different strength, and the wake dynamics are quite dissimilar. Here the smaller vortices are stretched by the induced velocity of the larger vortex pairs, resulting in what appears much more like a von Kármán vortex street (but again with upstream-tilted vortex pairs indicative of drag). For this combination of  $k$  and  $h$ , the fully laminar results are clearly the better match for the observed wake.

Figure 8 shows a comparison of experimental results at  $k \approx 4.0$ ,  $h = 0.025$  and numerical results at  $k = 4.0$ ,  $h = 0.025$  and  $k = 4.0$ ,  $h = 0.02$ . The experimental results show a neutral wake, where the

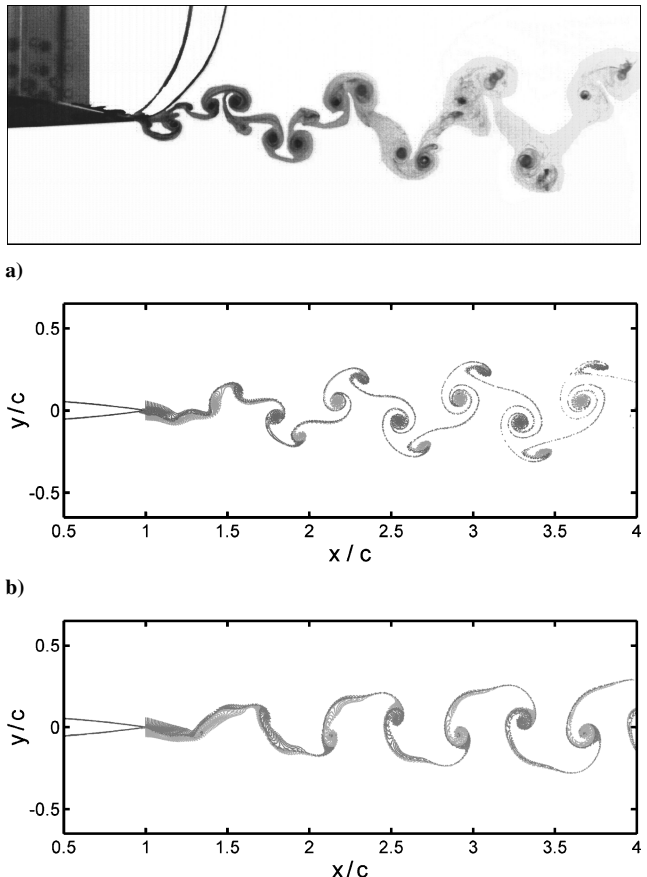


Fig. 7 Wake comparison: a) experimental  $k = 3.93$ ,  $h = 0.0125$ ; and numerical  $k = 4.0$ ,  $h = 0.0125$ ; b) laminar and c) turbulent.

thrust developed by the airfoil motion is balanced by the inherent drag, resulting in no net thrust, and untilted vortex mushrooms. Here again we see a marked difference in the numerical results between fully laminar and fully turbulent cases in the overall shape of the wake. The laminar results clearly show two same-sign vortices shed per half-cycle of airfoil motion, whereas the turbulent results have the same form as for  $h = 0.0125$ , where the second same-sign vortex is greatly reduced in size and stretched by the action of the larger vortices. The laminar numerical results at  $h = 0.02$  are a better match for the experimental visualization than at  $h = 0.025$  because they show similar position and relative size of shed vortices, as well as similar wake dynamics in that vortex pairs start to move through one another via self-induced velocities. The experimental behavior has been reproduced qualitatively in that a neutral wake is produced, although at a lower oscillation amplitude than in the experiment. Similar results were observed for calculations made at both  $M_\infty = 0.05$  and  $M_\infty = 0.2$ , with different levels of grid refinement.

Figure 9 compares experimental and numerical results at  $k \approx 4.0$  and  $h = 0.05$ . For both the laminar and turbulent numerical results, a close similarity with the experimental visualization is apparent in terms of the large-scale shape of the wake, with downstream-tilted vortex pairs indicative of net thrust (confirmed by averaged flowfield calculations showing a jet aft of the trailing edge). For this case, little difference between laminar and turbulent results is discernable.

Figure 10 shows a comparison of experimental and numerical results at  $k \approx 4.0$  and  $h = 0.075$ . Again a close large-scale similarity with the experimental visualization is apparent for both laminar and turbulent numerical results. Helmholtz shear layer instability vortices are visible in between the large shed vortices. Fully turbulent numerical results are very similar on the large scale, but the shear layer instability is not as prominent.

Figure 11 shows a comparison of experimental and numerical results at  $k \approx 8.0$ ,  $h = 0.0125$ . The macroscopic wake structure is well

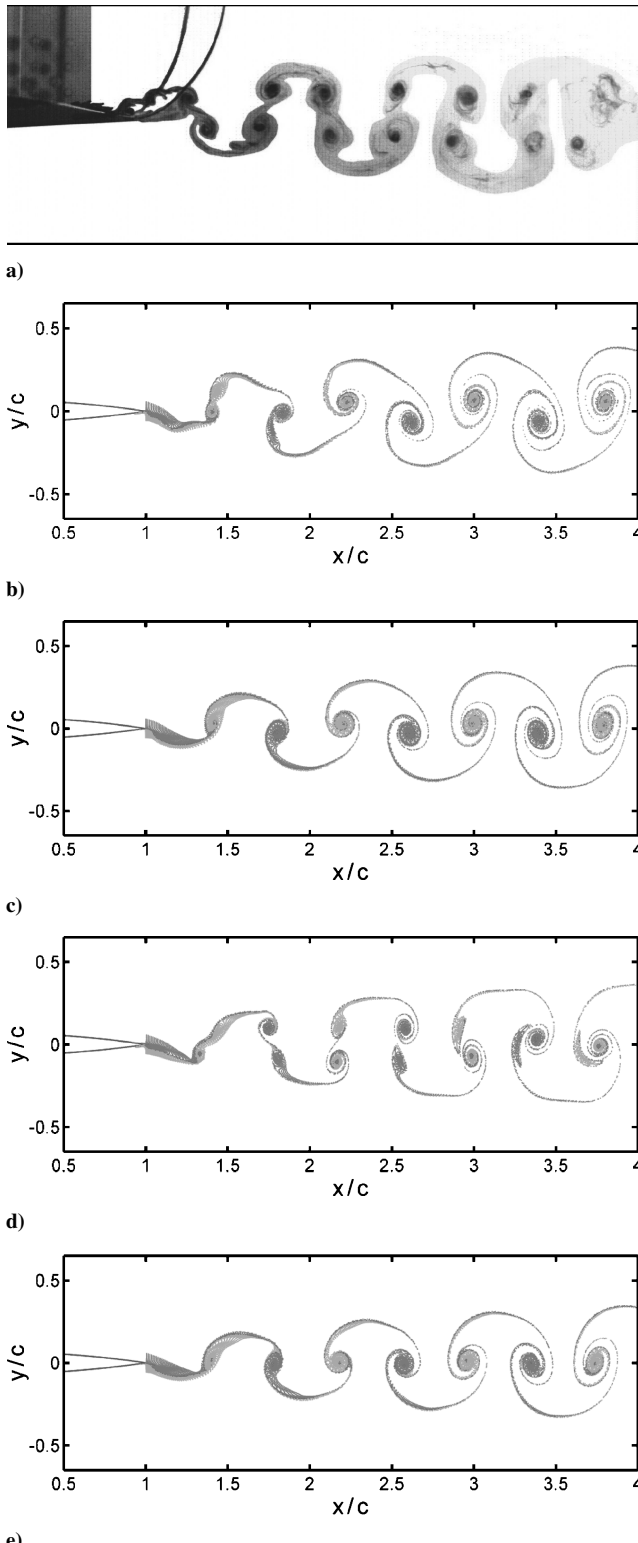


**Fig. 8** Wake comparison: a) experimental  $k = 3.93$ ,  $h = 0.025$  and b) numerical  $k = 4.0$ ,  $h = 0.025$ , laminar and c) turbulent, and numerical  $k = 4.0$ ,  $h = 0.02$ , d) laminar and e) turbulent.

approximated by both the laminar and turbulent numerical results. When Figs. 11 are compared to the results in Fig. 8, produced at half the reduced frequency but with the same value of  $kh$ , we see a marked difference in the wake structure. The results presented in Figs. 7–11 also compare well to other experimental wake visualizations in the literature.<sup>19,20</sup>

The agreement between the experimental and numerical laminar results at the lower plunge amplitudes is more likely to be an

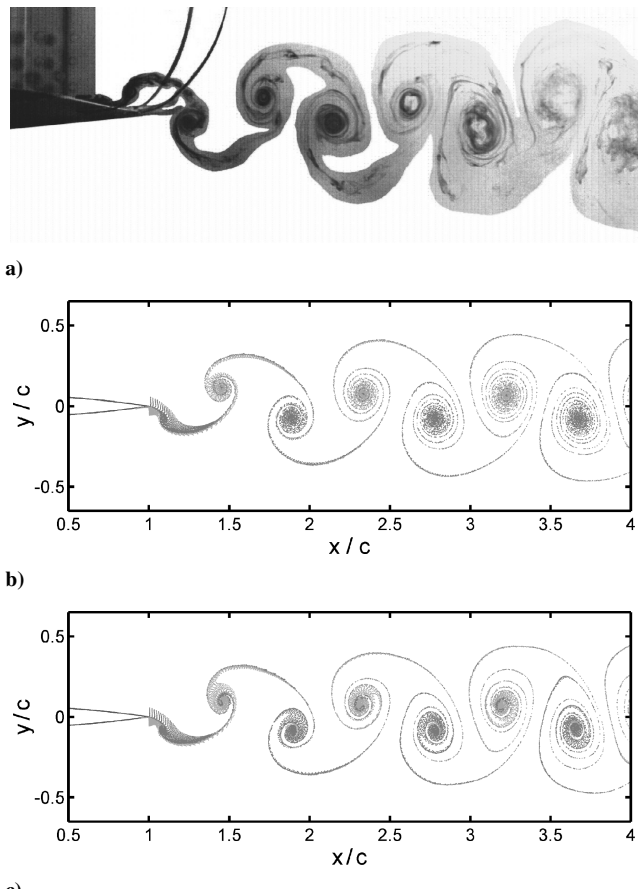


**Fig. 9** Wake comparison: a) experimental  $k = 3.93$ ,  $h = 0.05$ ; and numerical  $k = 4.0$ ,  $h = 0.05$ ; b) laminar and c) turbulent.

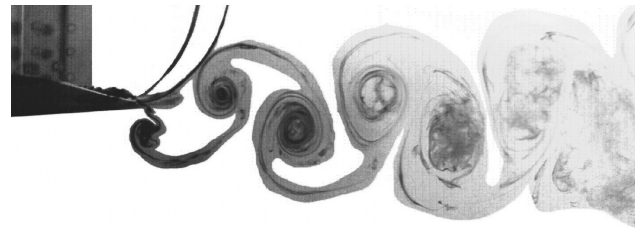
indication that the flow in the experiments of Lai and Platzer<sup>17</sup> was laminar than that the turbulence model is doing a poor job of predicting the flow. Convergence of laminar and turbulent results for larger amplitudes is discussed later in the Effect of Turbulence Model and Numerical Viscosity section.

#### Dependence of Wake Structure on Plunging Frequency and Amplitude

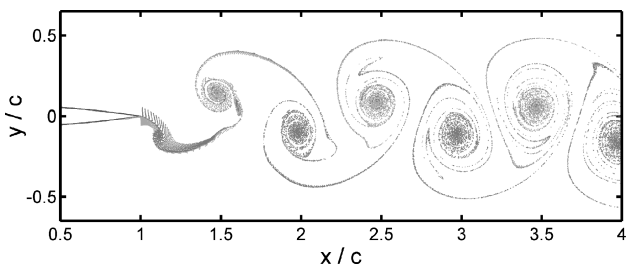
Figure 12 shows a comparison of three numerical laminar wakes produced at  $kh = 0.05$ , but with varying  $k$  and  $h$ . The wakes are shown at the same equivalent scale (normalized against single-sided plunge amplitude  $a$ ). We see a straightforward von Kármán vortex street at  $k = 8.0$ ,  $h = 0.00625$ , but much more complicated multiple-vortex-per-half-cycle-type shedding at  $k = 4.0$ ,  $h = 0.0125$  and  $k = 2.0$ ,  $h = 0.025$ . Figure 13 shows the same plunging frequencies, but with  $kh = 0.1$ , and again there is a marked difference in wake structures. In Figs. 12 and 13, the normalized wavelength of the wake remains approximately the same as  $k$  is varied, but the distribution of vorticity shed into the wake throughout the plunge cycle varies. This supports the assertion made in the Linearized Analysis section that  $kh$  is not the sole determinant of wake structure. The good agreement between experimental and laminar numerical results for the range of  $k$  and  $h$  presented in this paper increases confidence that the features observed in Figs. 12 and 13 are physically realistic. The following section provides an explanation for the complicated wake structures seen here.

#### Trailing-Edge Separation Effects

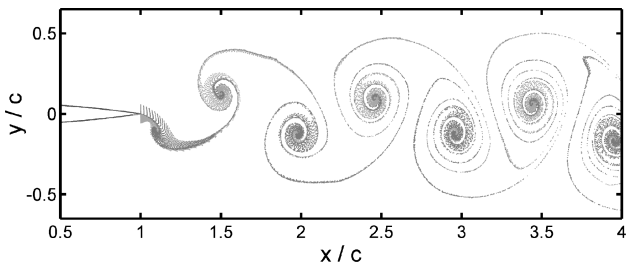
Figure 14 provides a closeup on the trailing edge at one instant in the plunge cycle, for  $k = 4$ ,  $h = 0.0125$ , fully laminar flow, showing instantaneous streamlines and the corresponding scalar particle trace. Animations of the flow structure at the trailing edge throughout the plunge cycle show separation regions on either or both sides of the airfoil, around which the remainder of the fluid flows, creating an effectively blunt-edged body. This may be seen in Fig. 14.



a)



b)



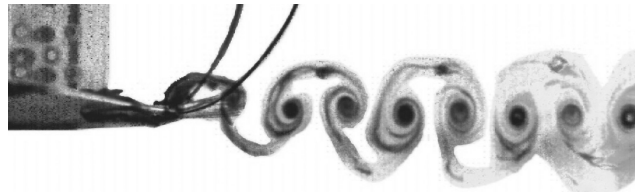
c)

**Fig. 10 Wake comparison: a) experimental  $k = 3.93$ ,  $h = 0.075$ ; and numerical  $k = 4.0$ ,  $h = 0.075$ : b) laminar and c) turbulent.**

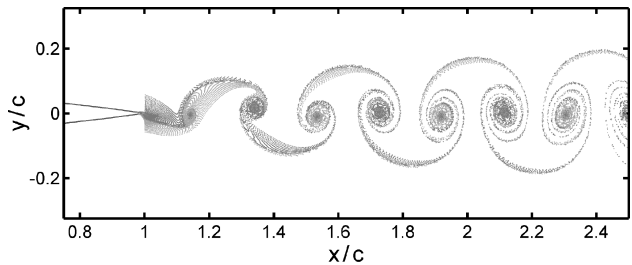
The degree of effective bluntness of the airfoil trailing edge varies throughout the plunge cycle, as well as with  $k$  and  $h$ . The trailing edge of the airfoil, now acting as a bluff body, will have a natural-shedding frequency associated with it, which will vary somewhat with the Reynolds number. (See Hannemann and Oertel,<sup>29</sup> for example, who showed natural shedding for a flat plate of finite-thickness, end-on to the flow.) Interaction of this natural-shedding mode with the vortex shedding associated with the airfoil plunge frequency appears to be the origin of the multiple-vortex-per-half-cycle shedding apparent in Figs. 7, 8, 12, and 13. The apparent invalidity of the Kutta condition (streamlines flowing around a reversed-flow separated region rather than smoothly leaving from the trailing edge on both sides) casts doubt on the assertion by Triantafyllou et al.<sup>6</sup> that phase locking of this shedding frequency and the plunge frequency (or a higher harmonic) will not be present.

### Quantitative Lift and Thrust Results

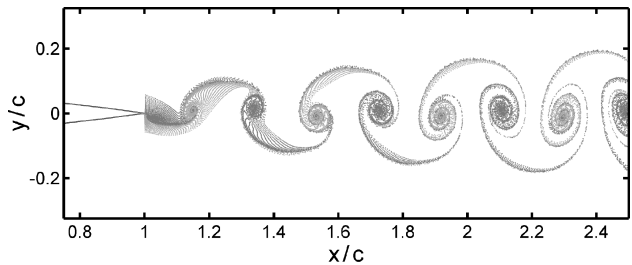
Figure 15 shows the time-averaged thrust coefficient predicted by the Garrick flat plate potential flow analysis<sup>14</sup> and by the UPM code for a NACA 0012 airfoil. It also shows the thrust predicted by the N-S code for a NACA 0012 airfoil for freestream Mach numbers  $M_\infty = 0.2$  and  $0.05$  and Reynolds number  $Re = 2 \times 10^4$ . The flow is assumed to be completely laminar, which is supported by the qualitative comparison of the wake structures with earlier experiment. The plunging frequency  $k$  and plunge amplitude  $h$  are varied to keep their product constant at  $kh = 0.3$ . Previous studies<sup>6</sup> have postulated that Strouhal number  $Sr$  (and here  $kh$ ) is the sole parameter that determines thrust for both pitching and plunging, although the recent work by Ramamurti and Sandberg<sup>25</sup> suggests there may be some frequency dependence at higher pitching frequencies. Bandyopadhyay et al.<sup>7</sup> also show a frequency dependence as well as Strouhal number dependence, for thrust generated by a flapping foil on a fishlike body.



a)



b)



c)

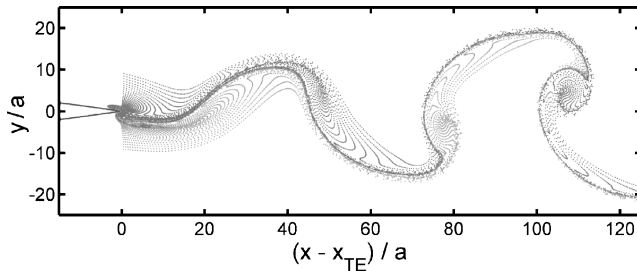
**Fig. 11 Wake comparison: a) experimental  $k = 7.85$ ,  $h = 0.0125$ ; and numerical  $k = 8.0$ ,  $h = 0.0125$ : b) laminar and c) turbulent.**

We see that, as discussed earlier, the mean thrust coefficient predicted by the Garrick analysis<sup>14</sup> asymptotes to a constant value dependent on  $kh$  alone, for  $k > 4$  to  $5$ . Below this frequency, there is significant variation with both  $k$  and  $h$ . We can determine the effect of some of the assumptions inherent in the Garrick analysis. First, the wake, consisting of vorticity shed from the trailing edge and confined to a narrow width rectilinear region behind the airfoil, is frozen in that it is not allowed to evolve in response to the self-induced velocities created by the wake vorticity. The UPM code removes this restriction by allowing wake evolution and nonlinear vortex wrapup. It also simulates a finite-thickness airfoil rather than a flat plate. However, the flow is assumed still to be incompressible and inviscid, and the Kutta condition is still enforced at the trailing edge, so that no separation is allowed anywhere on the airfoil surface.

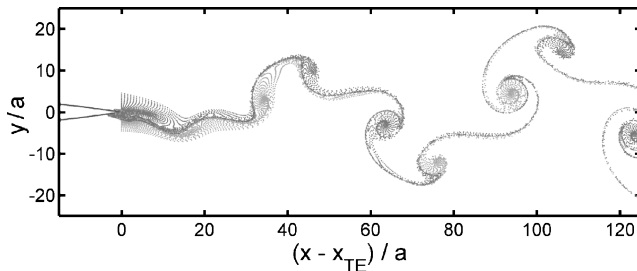
We can see from Fig. 15 that the UPM results fairly closely match the Garrick analysis,<sup>14</sup> including the decrease in thrust as frequency is increased, and an asymptotic approach to a constant value, but with a slightly lower asymptotic value. This may be attributed to that the wake becomes increasingly nonlinear with increasing frequency, in that the vortex wrapup takes place faster and closer to the airfoil trailing edge, thus, having more effect on the velocities over the airfoil surface.

The N-S code includes viscosity and the possibility of flow separation. Results were calculated for freestream Mach numbers of  $M_\infty = 0.2$  and  $0.05$ . As was determined in the pitching airfoil validation presented earlier, here for plunging motion with  $M_\infty = 0.2$ , as the frequency increases, compressibility effects become apparent. For  $M_\infty = 0.2$ ,  $kh = 0.3$ , peak Mach numbers were  $M_{\max} = 0.66$  ( $k = 2$ ),  $0.70$  ( $k = 4$ ), and  $0.56$  ( $k = 8$ ), indicating significant compressibility effects. For  $M_\infty = 0.05$ , the same plunge parameters gave  $M_{\max} = 0.15$ ,  $0.16$ , and  $0.21$ .

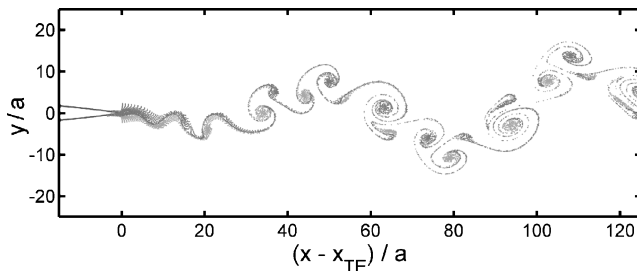
The results at  $M_\infty = 0.05$  show a reasonable match with the asymptotic trend of the Garrick<sup>14</sup> and UPM results at higher



a)



b)



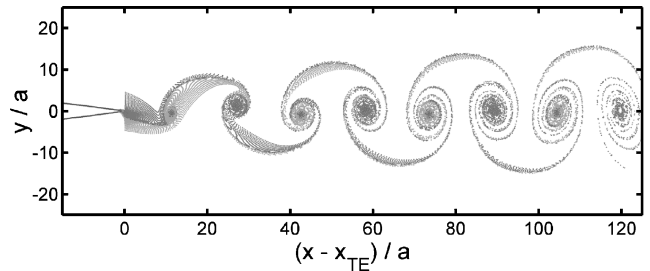
c)

Fig. 12 Numerical laminar: a)  $k = 8.0$ ,  $h = 0.00625$ ; b)  $k = 4.0$ ,  $h = 0.0125$ ; and c)  $k = 2.0$ ,  $h = 0.025$ .

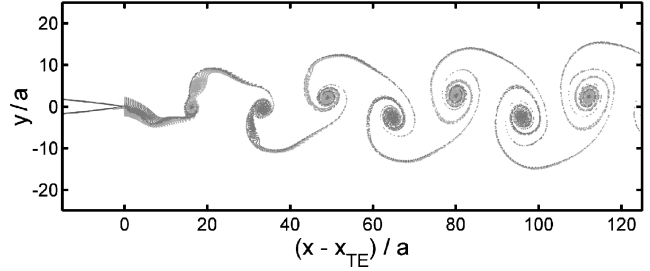
frequency, indicating that, for high enough frequency, the thrust does indeed become approximately independent of  $k$  and  $h$  separately and dependent only on  $kh$ . However, the trend at low frequency is the opposite of that for Garrick and UPM, in that the thrust decreases as the frequency is reduced. This might be expected because the small amplitude assumption inherent in the Garrick analysis is increasingly in error as the frequency decreases, with  $kh$  held constant. However, the UPM code, which allows arbitrary motions, reproduces the Garrick trend, so another explanation must be sought.

The plunging motion of the airfoil is sinusoidal about the neutral position, and the downstroke and upstroke produce the same magnitude of vertical force (with opposite sign), and so peak rather than mean values are examined when considering the lift forces generated. Figure 16 shows the peak lift coefficient achieved during the plunging cycle, as predicted by the Garrick analysis,<sup>14</sup> as well as the UPM code and the N-S code for  $M_\infty = 0.2$  and  $0.05$ . The Garrick result shows some initial decrease in lift with increasing frequency, then an asymptotic approach to a linear variation with frequency. The UPM code reproduces both these trends, but with marginally less peak lift predicted at a given frequency. The N-S results at  $M_\infty = 0.05$  also reproduce these trends, although with higher lift predicted at the higher frequencies.

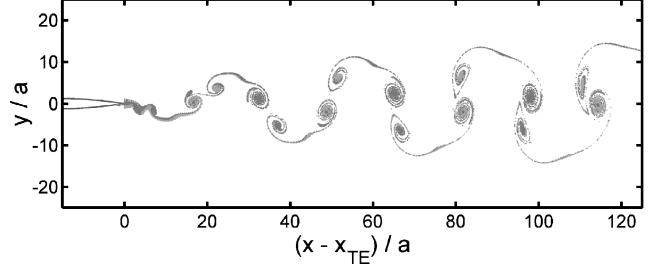
Thus, the N-S code (at  $M_\infty = 0.05$ ) predicts much lower thrust, but approximately the same lift, at the low plunging frequencies. The reason for this behavior is established by an examination of the pressure coefficient on the airfoil surface. Figure 17 shows the pressure distribution on the airfoil surface for  $k = 2, 4$ , and  $8$  (with  $kh$  held constant at  $0.3$ ). Shown are UPM and N-S  $M_\infty = 0.05$  results at the top of the upstroke in each case. Figure 17 shows a sharp dip in pressure near the leading edge, caused by vortex separation, which grows less pronounced as the plunging frequency increases.



a)



b)



c)

Fig. 13 Numerical laminar: a)  $k = 8.0$ ,  $h = 0.0125$ ; b)  $k = 4.0$ ,  $h = 0.025$ ; and c)  $k = 2.0$ ,  $h = 0.05$ .

For the  $k = 2$  case, the vortex still exhibits a significant influence on the airfoil as it passes over the point of maximum airfoil thickness. At this time, the contribution of the low pressure associated with the vortex will change sharply from thrust to drag, but with little effect on the lift. In this way, leading-edge separation appears to cause the reduction in thrust coefficient for  $k < 4$ . Leading-edge separation is still apparent at higher  $k$ , but the effect on lift and thrust is less important as the magnitude of the pressure coefficients generated over the airfoil surface increases with increasing  $k$ . The increase in pressure coefficient range with increasing  $k$  is matched by the UPM results shown in Fig. 17. This is consistent with the Garrick prediction in expression (1) and the results shown in Figure 16 that the peak lift increases with  $k$ .

### Effect of Turbulence Model and Numerical Viscosity

The simple algebraic turbulence model<sup>22</sup> used in the calculations, although with a limited range of applicability, was chosen primarily for its simplicity of implementation and widespread use. The intent of the turbulent calculations is to assess the susceptibility of the results to changes in leading- and trailing-edge separation, rather than to predict accurately the aerodynamic forces due to turbulence. The action of the turbulence model is to increase the effective viscosity in regions of high vorticity. For  $Re = 2 \times 10^4$ ,  $M_\infty = 0.05$ ,  $k = 4$ , and  $h = 0.0125$ , the turbulent viscosity either side of the airfoil trailing edge reaches approximately 10 times the freestream laminar viscosity, and for  $k = 4$ ,  $h = 0.075$ , it is approximately 60 times higher. This substantially alters the extent of the trailing-edge separation region. For the larger airfoil plunging amplitude, this has little effect because the flow over the trailing edge is dominated by the large-scale motion of the airfoil and is effectively forced to flow off the sharp trailing edge, so that the laminar and turbulent wakes

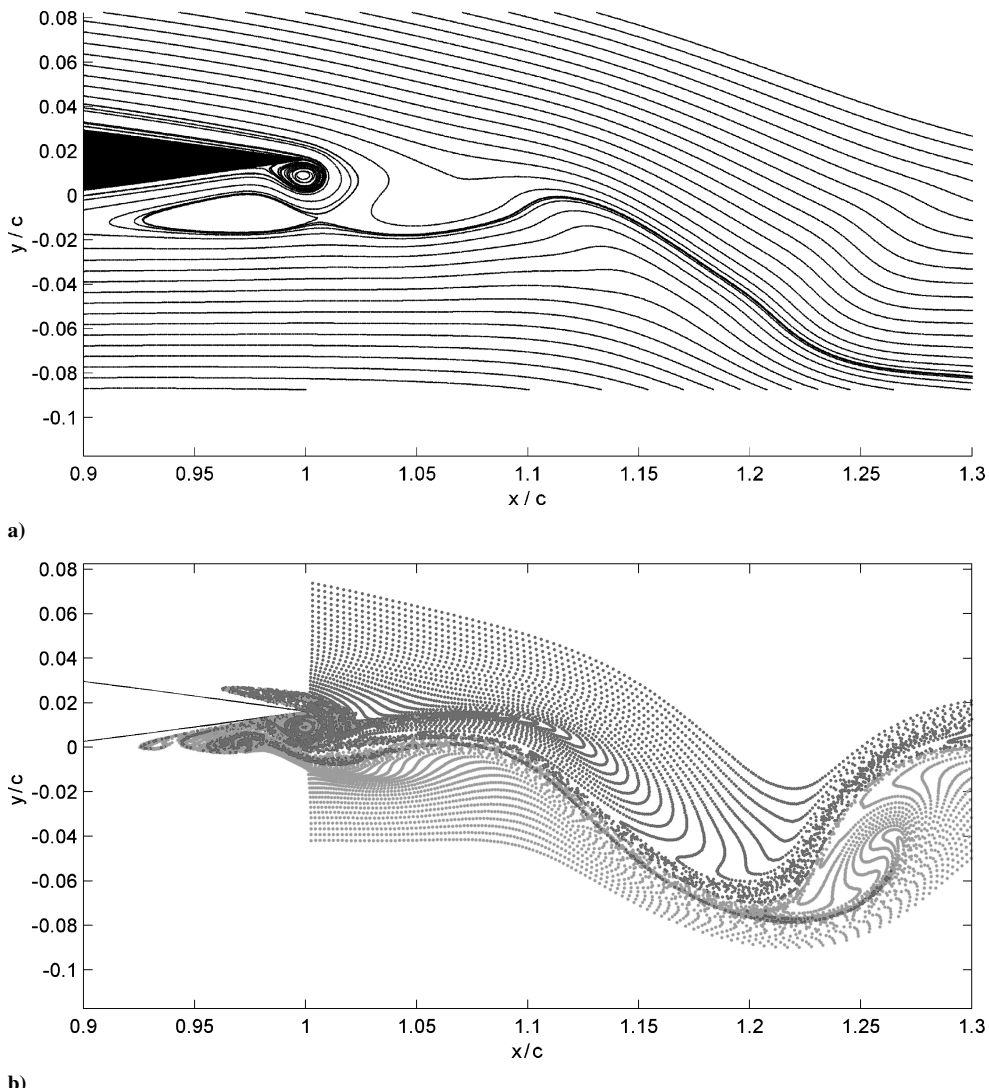


Fig. 14 Numerical laminar  $k = 4.0$ ,  $h = 0.0125$ , airfoil moving upward: a) instantaneous streamlines (velocity field relative to the airfoil) and b) corresponding particle trace snapshot.

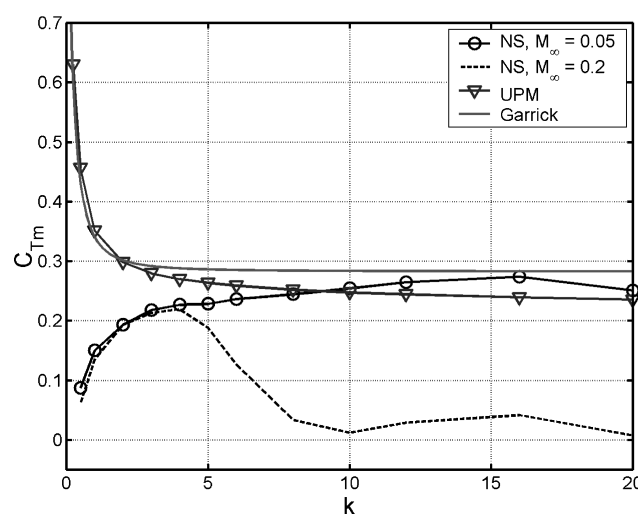


Fig. 15 Mean thrust coefficient vs reduced frequency, N-S ( $Re = 2 \times 10^4$ , laminar), UPM, and Garrick<sup>14</sup> analysis results, NACA 0012, plunging motion,  $kh = 0.3$ .

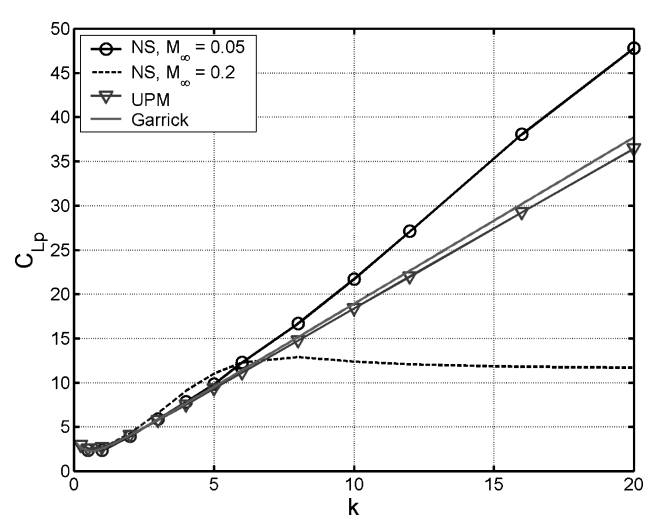


Fig. 16 Peak lift coefficient vs reduced frequency, N-S ( $Re = 2 \times 10^4$ , laminar), UPM, and Garrick<sup>14</sup> analysis results, NACA 0012, plunging motion,  $kh = 0.3$ .

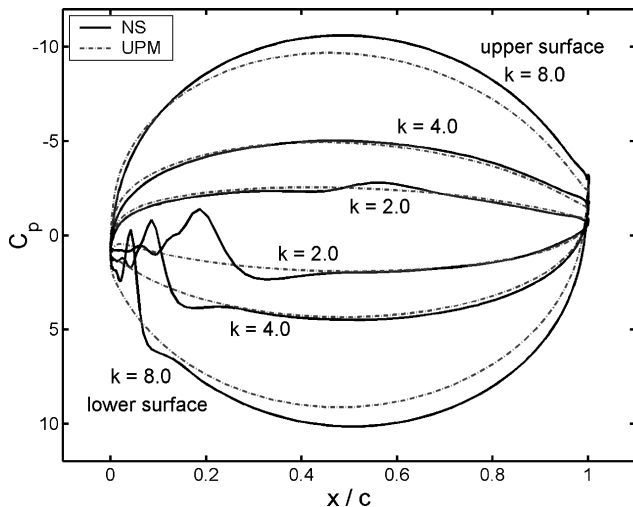


Fig. 17 Airfoil surface pressure distributions, N-S ( $Re = 2 \times 10^4$ ,  $M_\infty = 0.05$ , laminar) and UPM results, NACA 0012, plunging motion,  $kh = 0.3$ , airfoil at top of stroke in each case.

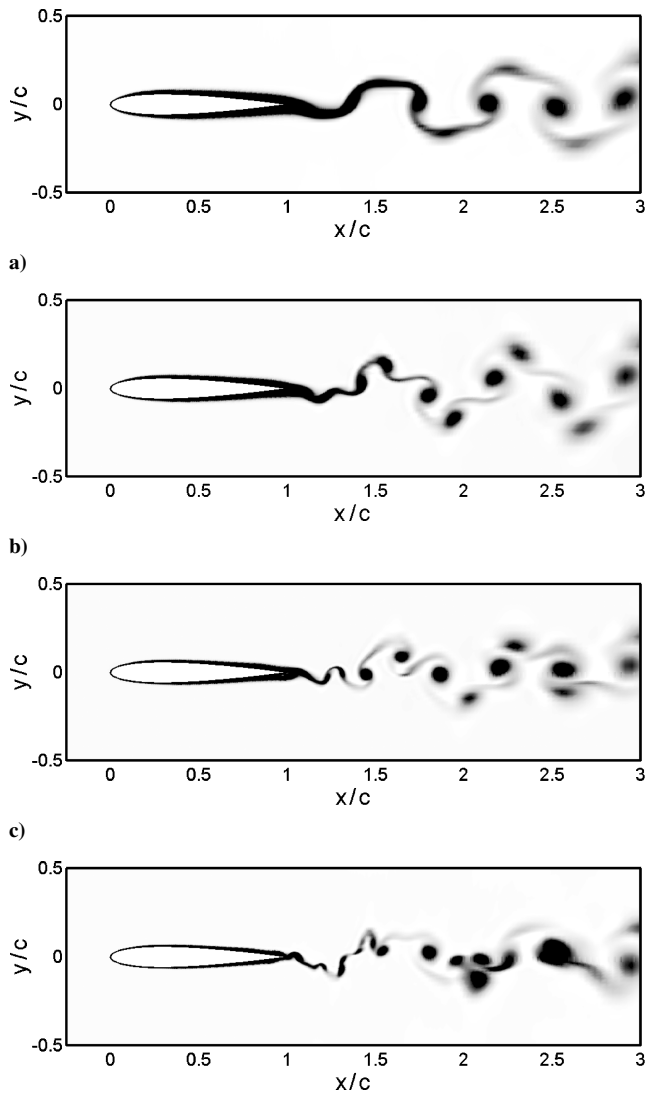


Fig. 18 Entropy filled-contour plots, plunging airfoil, laminar,  $k = 4.0$  and  $h = 0.0125$ : a)  $Re = 1 \times 10^4$ , b)  $Re = 2 \times 10^4$ , c)  $Re = 4 \times 10^4$ , and d)  $Re = 8 \times 10^4$ .

appear very similar. For the smaller plunge amplitude, altering the trailing-edge separation has a dominant effect on the appearance of the wake, due to interaction between the plunge frequency and the frequency of vortex shedding off the separated region, which is of the same order of magnitude size as the airfoil motion. Thus, the laminar and turbulent cases give rise to very different wakes at small plunge amplitudes and high frequencies, but similar wakes at large amplitudes and lower frequencies. In this way, the structure of the wake is dominated by trailing-edge effects.

In contrast, the aerodynamic forces on the airfoil were found to be only marginally affected by whether the flow is assumed laminar or turbulent (results not presented here due to space limitations), except at the very lowest frequencies considered (where leading-edge separation is most prominent). This further supports the idea that the aerodynamic forces at this Reynolds number are dominated by leading edge-, rather than trailing-edge effects, as already revealed in Fig. 17.

The sensitivity of the wake to the additional viscosity introduced by the turbulence model suggests that numerical viscosity is low, at least close to the airfoil where the wake vortices are created. This idea is reinforced by Fig. 18, which shows a comparison of results for  $k = 4$ ,  $h = 0.0125$  at Reynolds numbers of  $1 \times 10^4$ ,  $2 \times 10^4$ ,  $4 \times 10^4$  and  $8 \times 10^4$  with laminar flow assumed. Significant variation in the size of the trailing-edge separation region, and hence the vortex shedding and wake structure, is observed. Again the apparent sensitivity of the results to this effective change (doubling, halving, and quartering) in freestream viscosity suggests that the results presented here are being governed by physical effects rather than numerical viscosity.

## Conclusions

The wake of a two-dimensional NACA 0012 airfoil oscillated sinusoidally in plunge is simulated with a compressible Reynolds averaged N-S flow solver, with both fully laminar and fully turbulent flow assumptions.

Validation of the N-S code against pitching airfoil results show that the freestream Mach number used in the simulations has an important effect on the forces predicted. This is also seen in the plunging airfoil results. However, reducing the Mach number does not significantly influence the wake structures observed in the simulations, other than to increase the level of grid refinement necessary to obtain matches to experimentally observed structures. Comparison of fully laminar and fully turbulent plunging airfoil simulations shows very different wake structures due to different trailing-edge flow behavior, but aerodynamic forces differ significantly only where leading-edge separation is prominent. These results, as well as the surface pressure coefficient distributions shown in Fig. 17, indicate that leading-edge effects are of primary importance in determining the forces developed by the plunging airfoil at this Reynolds number. Trailing-edge effects have a strong influence on the observed wake structures, but only a secondary effect on lift and thrust.

The laminar wake structure results closely reproduce the experimental results of Lai and Platzer<sup>17</sup> and agree with experimental results in the literature,<sup>6,19,20</sup> that is, a change from a von Kármán vortex street or multiple-vortex-per-half-cycle wake patterns for drag-producing conditions, through more complicated vortex structures as the neutral thrust condition is approached, to a reverse von Kármán vortex street for thrust-producing conditions. Close agreement is obtained for a range of plunge frequencies and amplitudes. In general, the laminar simulations are a better match for the observed wake structures, both in terms of individual features at a given combination of  $k$  and  $h$  and changes in wake structure across a range of  $k$  and  $h$ . Also the wake structure simulations and thrust calculations carried out at constant  $kh$  show that this cannot be the single parameter controlling the flow, but that  $k$  and  $kh$  must be treated separately for  $k < 4$  approximately and for the Reynolds number under consideration.

## Acknowledgment

This work was supported by an award under the Merit Allocation Scheme on the National Facility of the Australian Partnership for Advanced Computing.

## References

- <sup>1</sup>Katz, J., and Weihs, D., "Behavior of Vortex Wakes from Oscillating Airfoils," *Journal of Aircraft*, Vol. 15, No. 12, 1978, pp. 861–863.
- <sup>2</sup>Choudhuri, P. G., Knight, D. D., and Visbal, M. R., "Two-Dimensional Unsteady Leading-Edge Separation on a Pitching Airfoil," *AIAA Journal*, Vol. 32, No. 4, 1994, pp. 673–680.
- <sup>3</sup>Ekaterinaris, J. A., and Platzer, M. F., "Computational Prediction of Airfoil Dynamic Stall," *Progress in Aerospace Sciences*, Vol. 33, 1997, pp. 759–846.
- <sup>4</sup>Isogai, K., Shinmoto, Y., and Watanabe, Y., "Effects of Dynamic Stall on Propulsive Efficiency and Thrust of Flapping Airfoil," *AIAA Journal*, Vol. 37, No. 10, 1999, pp. 1145–1151.
- <sup>5</sup>Lighthill, M. J., "A Note on the Swimming of Slender Fish," *Journal of Fluid Mechanics*, Vol. 9, 1960, pp. 305–317.
- <sup>6</sup>Triantafyllou, G. S., Triantafyllou, M. S., and Grosenbaugh, M. A., "Optimal Thrust Development in Oscillating Foils with Application to Fish Propulsion," *Journal of Fluids and Structures*, Vol. 7, 1993, pp. 205–224.
- <sup>7</sup>Bandyopadhyay, P. R., Castano, J. M., Nedderman, W. H., and Donnelly, M. J., "Experimental Simulation of Fish-Inspired Unsteady Vortex Dynamics on a Rigid Cylinder," *Journal of Fluids Engineering*, Vol. 122, No. 2, 2000, pp. 219–238.
- <sup>8</sup>Lai, J. C. S., Yue, J., and Platzer, M. F., "Control of Backward Facing Step Flow Using a Flapping Airfoil," *Experiments in Fluids*, Vol. 82, No. 1, 2002, pp. 44–54.
- <sup>9</sup>Tuncer, I. H., Lai, J. C. S., and Platzer, M. F., "A Computational Study of Flow Reattachment over a Stationary/Flapping Airfoil Combination in Tandem," AIAA Paper 98-0109, Jan. 1998.
- <sup>10</sup>Shy, W., Berg, M., and Ljungqvist, D., "Flapping and Flexible Wings for Biological and Micro Air Vehicles," *Progress in Aerospace Sciences*, Vol. 35, 1999, pp. 455–505.
- <sup>11</sup>Katzmayr, R., "Effect of Periodic Changes of Angle of Attack on Behavior of Airfoils," NACA TM-147, Oct. 1922; translated from *Zeitschrift für Flugtechnik und Motorluftschiffahrt*, 31 March 1922, pp. 80–82, and 13 April 1922, pp. 95–101.
- <sup>12</sup>Koochesfahani, M. M., "Vortical Patterns in the Wake of an Oscillating Airfoil," *AIAA Journal*, Vol. 27, No. 9, 1989, pp. 1200–1205.
- <sup>13</sup>Dohring, C. M., Platzer, M. F., Jones, K. D., and Tuncer, I. H., "Computational and Experimental Investigation of the Wakes Shed from Flapping Airfoils and Their Wake Interference/Impingement Characteristics," *Proceedings of the AGARD-FDP Symposium on the Characterisation and Modification of Wakes from Lifting Vehicles in Fluids*, AGARD CP-584, 1996, Chap. 33, pp. 1–9.
- <sup>14</sup>Garrick, I. E., "Propulsion of a Flapping and Oscillating Airfoil," NACA Rep. 567, May 1936.
- <sup>15</sup>Freymuth, P., "Propulsive Vortical Signature of Plunging and Pitching Airfoils," *AIAA Journal*, Vol. 26, No. 7, 1988, pp. 881–883.
- <sup>16</sup>Jones, K. D., Dohring, C. M., and Platzer, M. F., "Experimental and Computational Investigation of the Knoller–Betz Effect," *AIAA Journal*, Vol. 36, No. 7, 1998, pp. 1240–1246.
- <sup>17</sup>Lai, J. C. S., and Platzer, M. F., "Jet Characteristics of a Plunging Airfoil," *AIAA Journal*, Vol. 37, No. 12, 1999, pp. 1529–1537.
- <sup>18</sup>McCroskey, W. J., "Unsteady Airfoils," *Annual Review of Fluid Mechanics*, Vol. 14, 1982, pp. 285–311.
- <sup>19</sup>Ohashi, H., and Ishikawa, N., "Visualization Study of a Flow near the Trailing Edge of an Oscillating Airfoil," *Bulletin of the Japanese Society of Mechanical Engineers*, Vol. 15, 1972, pp. 840–845.
- <sup>20</sup>Kadlec, R. A., and Davis, S. S., "Visualization of Quasiperiodic Flows," *AIAA Journal*, Vol. 17, No. 11, 1979, pp. 1164–1169.
- <sup>21</sup>Tuncer, I. H., and Platzer, M. F., "Computational Study of Flapping Airfoil Aerodynamics," *Journal of Aircraft*, Vol. 37, No. 3, 2000, pp. 514–520.
- <sup>22</sup>Baldwin, B. S., and Lomax, H., "Thin Layer Approximation and Algebraic Model for Separated Turbulent Flows," AIAA Paper 78-257, Jan. 1978.
- <sup>23</sup>Basu, B. C., and Hancock, G. J., "The Unsteady Motion of a Two-Dimensional Aerofoil in Incompressible Inviscid Flow," *Journal of Fluid Mechanics*, Vol. 87, No. 1, 1978, pp. 159–178.
- <sup>24</sup>Jones, K. D., Dohring, C. M., and Platzer, M. F., "Wake Structures Behind Plunging Airfoils: A Comparison of Numerical and Experimental Results," AIAA Paper 96-0078, Jan. 1996.
- <sup>25</sup>Ramamurti, R., and Sandberg, W., "Simulation of Flow About Flapping Airfoils Using Finite Element Incompressible Flow Solver," *AIAA Journal*, Vol. 39, No. 2, 2001, pp. 253–260.
- <sup>26</sup>Volpe, G., "Performance of Compressible Flow Codes at Low Mach Numbers," *AIAA Journal*, Vol. 31, No. 1, 1993, pp. 49–56.
- <sup>27</sup>Milholen, W. E., Chokani, N., and Al-Saadi, J., "Performance of Three-Dimensional Compressible Navier–Stokes Codes at Low Mach Numbers," *AIAA Journal*, Vol. 34, No. 7, 1996, pp. 1356–1362.
- <sup>28</sup>Jones, K. D., and Platzer, M. F., "Numerical Computation of Flapping Wing Propulsion and Power Extraction," AIAA Paper 97-0826, Jan. 1997.
- <sup>29</sup>Hannemann, K., and Oertel, H., "Numerical Simulation of the Absolutely and Convectively Unstable Wake," *Journal of Fluid Mechanics*, Vol. 199, 1989, pp. 55–88.

K. Fujii  
Associate Editor